The Astronomical Journal, 168:117 (15pp), 2024 September https://doi.org/10.3847/1538-3881/ad597a

Electron Density Distribution in H II Regions in IC 10

Fiorella L. Polles[1], Dario Fadda[2], William D. Vacca[3], Nicholas P. Abel[4], Mélanie Chevance[5,6], Christian Fischer[7], James M. Jackson[8], Vianney Lebouteiller[9], Suzanne Madden[9], and Lise Ramambason[5]
[1] SOFIA Science Center, USRA, NASA Ames Research Center, M.S. N232-12 Moffett Field, CA 94035, USA; flpolles@gmail.com
[2] Space Telescope Science Institute, 3700 San Martin Drive, Baltimore, MD 21218, USA
[3] Gemini Observatory/NSF's NOIRLab, 950 N. Cherry Avenue, Tucson, AZ 85719, USA
[4] University of Cincinnati, Clermont College, 4200 Clermont College Drive, Batavia, OH 45103, USA
[5] Universität Heidelberg, Zentrum für Astronomie, Institut für Theoretische Astrophysik, Albert-Ueberle-Str 2, D-69120 Heidelberg, Germany
[6] Cosmic Origins Of Life (COOL) Research DAO, coolresearch.io, Germany
[7] Deutsche SOFIA Institut, University of Stuttgart, D-70569 Stuttgart, Germany
[8] Green Bank Observatory, P.O. Box 2, Green Bank, WV 24944, USA
[9] Université Paris-Cité, Université Paris-Saclay, CEA, CNRS, AIM, 91191, Gif-sur-Yvette, France
Received 2024 April 2; revised 2024 June 13; accepted 2024 June 14; published 2024 August 13

Abstract

We present the [O III] λ52 μm map of the dwarf galaxy IC 10 obtained with the Field-Imaging Far-Infrared Line Spectrometer on board the Stratospheric Observatory for Infrared Astronomy. We combine the [O III] λ52 μm map with Herschel and Spitzer observations to estimate the electron density distribution of the brightest H II regions of IC 10. We find that the line ratio [O III] λ88 μm/[O III] λ52 μm gives electron density (n_e) values ($n_{e\ [O\ III]}$) that cover a broad range, while the n_e values obtained using the line ratio [S III] λ33 μm/[S III] λ18 μm ($n_{e\ [S\ III]}$) are all similar within the uncertainties. $n_{e\ [O\ III]}$ is similar to $n_{e\ [S\ III]}$ for the M1, M2, and A1 regions, and it is higher than $n_{e\ [S\ III]}$ for the two regions, A2 and M1b, which are the brightest in the 24 μm continuum emission. These results suggest that for these regions, the two ions, O^{++} and S^{++}, trace two different ionized gas components and that the properties of the ionized gas component traced by the O^{++} ion are more sensitive to the local physical conditions. In fact, while the gas layer traced by [S III] does not keep track of the characteristics of the radiation field, the $n_{e\ [O\ III]}$ correlates with the star formation rate, the dust temperature, and the 24 μm. Therefore, $n_{e\ [O\ III]}$ is an indicator of the evolutionary stage of the H II region and the radiation field, with higher $n_{e\ [O\ III]}$ found in younger star-forming regions and in more energetic environments.

Unified Astronomy Thesaurus concepts: Interstellar medium (847); Dwarf galaxies (416)

1. Introduction

The gas density plays a role in many properties of the interstellar medium (ISM), such as the gas pressure, the electron temperature, the ionization parameter, and the elemental abundances (e.g., Rubin 1989; Rickards Vaught et al. 2024; Méndez-Delgado et al. 2024). The electron density (n_e) is often approximated to be constant inside the H II regions up to the ionization front when detailed information about the density is lacking (e.g., Cosens et al. 2022; Spinoglio et al. 2022). However, several studies have revealed that this assumption is incorrect: n_e can have a complex radial profile inside the H II regions. Some H II regions show density gradients (e.g., Rubin et al. 2011; McLeod et al. 2016), others show density fluctuations (e.g., Méndez-Delgado et al. 2023; Rickards Vaught et al. 2024). Moreover, integrated H II regions may include a mix of ionized gas layers with different densities, unresolved high-density clumps surrounded by lower-density ionized gas as well as filaments with different densities due to stellar feedback (e.g., O'Dell et al. 2017). The mix of gas densities is even more complex on the scale of a galaxy, especially for unresolved galaxies where all of the components are mixed within a spatial resolution element. The uncertainties in constraining n_e propagate to uncertainties on the derived physical properties of the ISM, such as thermal gas pressure, and on the derived stellar feedback mechanisms. Thus, an accurate knowledge of n_e is of fundamental importance to properly infer the structure and the properties of the ISM, as well as the interplay between the ISM and stars.

The electron density can be directly derived using ratios of lines emitted by two levels of the same ion with different critical densities and energy of the transition so that the excitation of these levels depends only on the density and the temperature of the gas (e.g., Osterbrock & Ferland 2006; Kewley et al. 2019b). Examples of line ratios that can be used to derive the electron density are [Si III] λ1883 Å/Si III] λ1892 Å and [C III] λ1906 Å/C III] λ1909 Å in the UV (e.g., Nussbaumer & Schild 1979; Keenan et al. 1992); [O II]λ3729 Å/3727 Å, [Ar IV]λ4711 Å/4740 Å, and [S II]λ6716 Å/6731 Å in the optical (e.g., Kaasinen et al. 2017; Della Bruna et al. 2020); and [O III] λ88 μm/52 μm, [Ne III]λ 36 μm/15 μm, and [N II]λ 205 μm/122 μm in the infrared (IR; e.g., Pineda et al. 2019; Chevance et al. 2020; Peng et al. 2021). Based on the ionization potentials (IPs) and critical densities, the lines may arise from different components of H II regions. Considering the H II region as a single slab of gas illuminated by a stellar cluster, the ionization lines such as [Ne III]λ 36 μm and [Ne III]λ 15 μm (IP 40.96 eV) trace the ionized gas close to the ionizing source, while the lines with lower excitation potential, such as [N II]λ 122 μm and [N II]λ 205 μm (IP 14.53 eV), trace the ionization front (e.g., Kewley et al. 2019b). Moreover, each electron density diagnostic is sensitive only to the density range below the critical densities of the lines of the ratio. Hence, we may expect to determine different density

values for different line ratios, providing a convenient means to determine the density structure of the ionized gas (e.g., Rubin et al. 2011; Fernández-Ontiveros et al. 2016). The best density indicators are those for which the derived value depends only very weakly on the temperature, which is why low-lying forbidden lines are the best (e.g., Spinoglio et al. 2015; Kewley et al. 2019b). Moreover, IR lines are less affected by extinction by dust than optical lines. Therefore, IR fine-structure line ratios emitted by the same ion are excellent density tracers. The IR wavelength domain provides several electron density diagnostics, each of them covering a different and complementary density range, e.g., [N II] traces a density range of $1-100\ \mathrm{cm}^{-3}$, [O III] traces 10–$10^3\ \mathrm{cm}^{-3}$, [S III] traces a range between 100 and $10^4\ \mathrm{cm}^{-3}$, and the [Ar III] and [Ne III] lines are useful between 10^3 and $10^5\ \mathrm{cm}^{-3}$ (e.g., Osterbrock & Ferland 2006).

Ideal laboratories to investigate the electron density distribution using IR diagnostics are nearby galaxies. Here we focus on the dwarf galaxy IC 10. Despite the low metallicity of $12+\log(\mathrm{O/H})=8.26$ ($\approx 1/3$ solar; e.g., Lequeux et al. 1979; Magrini & Goncalves 2009), this galaxy has a high surface density of Wolf–Rayet (WR) stars (e.g., Massey & Holmes 2002; Tehrani et al. 2017) and an unexpected high ratio of carbon-type WR (WC) to nitrogen-type WR (WN), indicating its starburst nature (e.g., Crowther et al. 2003). Due to these characteristics and its proximity ($\sim$715 kpc; e.g., Kim et al. 2009), IC 10 has been observed with several instruments, covering a broad range of wavelengths. The rich data set extends from X-ray to radio, allowing the characterization of the stellar population (e.g., Crowther et al. 2003; Vacca et al. 2007) and the physical and kinematic properties (e.g., López-Sánchez et al. 2011; Cosens et al. 2022) of the several H II regions (Hodge et al. 1991), as well as the neutral (e.g., Ashley et al. 2014) and molecular gas (e.g., Kepley et al. 2018) of the galaxy. The properties of the ionized gas of IC 10 have been investigated in a previous paper (Polles et al. 2019) through models of the mid-IR (MIR) and far-IR (FIR) Spitzer and Herschel fine-structure lines. That study revealed that most of the H II regions have almost identical physical properties (density, ionization parameter, and age of the stellar cluster), and they are all matter bounded. However, the analysis of the physical properties of the H II regions was limited by the availability of a single tracer of electron density, [S III] $\lambda 33\ \mu$m/[S III] $\lambda 18\ \mu$m. The lack of a variety of density tracers might have prevented us from unveiling the density structure of the H II regions, which could have been used to constrain and quantify the stellar feedback processes and reveal the evolution of H II regions, assuming a single density could lead to incorrect conclusions regarding, for example, the determination of the elemental abundances. In this paper, we present the new [O III] $\lambda 52\ \mu$m map of IC 10 observed with the Stratospheric Observatory for Infrared Astronomy (SOFIA; Erickson & Davidson 1993), and we analyze the electron density structure of the brightest H II regions of the galaxy, combining the SOFIA data with Herschel and Spitzer data.

The structure of the paper is the following: in Section 2 we describe the data, and in Section 3 we estimate the electron density distribution using the line ratios [O III] $\lambda 88\ \mu$m/[O III] $\lambda 52\ \mu$m and [S III] $\lambda 33\ \mu$m/[S III] $\lambda 18\ \mu$m. The results and their implications are discussed in Section 4. Finally, Section 5 summarizes the main points of this study.

Table 1
Characteristics of the Observations

Tracer	Wavelength (μm)	FWHM (arcsec)	Pixel size (arcsec)
Hα	0.6563	2.2	0.5
[S III]	18.7	12	12
[S III]	33.5	12	12
[O III]	51.8	6.6	2
[O III]	88.4	9.5	3
MIPS_24	24	6	1.5
PACS_70	70	5.6	2
PACS_100	100	6.8	3

2. Data

The characteristics of the observations used in this study are presented in Table 1, and the maps are shown in Figure 1. The general properties of the IR fine-structure lines used to calculate n_e are summarized in Table 2.

2.1. SOFIA/FIFI-LS data

2.1.1. Observations

IC 10 has been observed with the Far Infrared Field-Imaging Line Spectrometer (FIFI-LS; Fischer et al. 2018; Colditz et al. 2018) on board SOFIA as part of the GTO program 70_0908 (P.I.: Alfred Krabbe), during two flights, 2022 August 31 and 2022 September 1, flying out of Palmdale, California.

FIFI-LS is an integral-field FIR spectrometer, providing a spectrum at each pixel in its field of view, with a spectral resolution from 500 to 2000 from 51 to 203 μm. This instrument includes two channels for simultaneous observations: the blue channel covering the wavelength range 51–120 μm and the red channel observing between 115 and 203 μm.Each channel has a 5×5 pixel projection on the sky. For the blue channel, the pixel size is $6''\times 6''$; for the red channel, it is $12''\times 12''$. For each spatial pixel (also called "spaxel"), the light is dispersed spectrally over 16 pixels, providing an integral-field data cube for each observation, covering a total spectral bandwidth between 1500 and 3000 $\mathrm{km\,s}^{-1}$, depending on the wavelength. The light is dispersed by ruled gratings mounted to a tilting drive and reimaged onto a detector of stressed gallium doped germanium photoconductors.

The two main star-forming regions of IC 10 (see Figure 1) have been covered in [O III] $\lambda 52\ \mu$m with the blue channel and [O I] $\lambda 145.5\ \mu$m with the red channel. In this paper, we focus on the [O III] $\lambda 52\ \mu$m observations. The data were acquired in symmetric chop mode, i.e., the sky background positions are located across the optical axis from source position,[10] for maximum observing efficiency (Fischer et al. 2016). A chop throw of $4'$ toward the northwest as well as southeast direction was chosen to safely chop out of the galaxy. The total wall-clock time of the [O III] $\lambda 52\ \mu$m was about 5.5 hr. Four blue channel $30''\times 30''$ fields where pointed to regions with bright [O III] $\lambda 88\ \mu$m emission previously identified with Herschel/Photodetector Array Camera and Spectrometer (PACS; see Section 2.2.1) to create the map shown in Figure 1. Additional subpixel dithering was performed to improve spatial sampling.

[10] See https://irsa.ipac.caltech.edu/data/SOFIA/docs/instruments/handbooks/FIFI-LS_Handbook_for_Archive_Users_Ver1.0.pdf, Section 2.4.1.

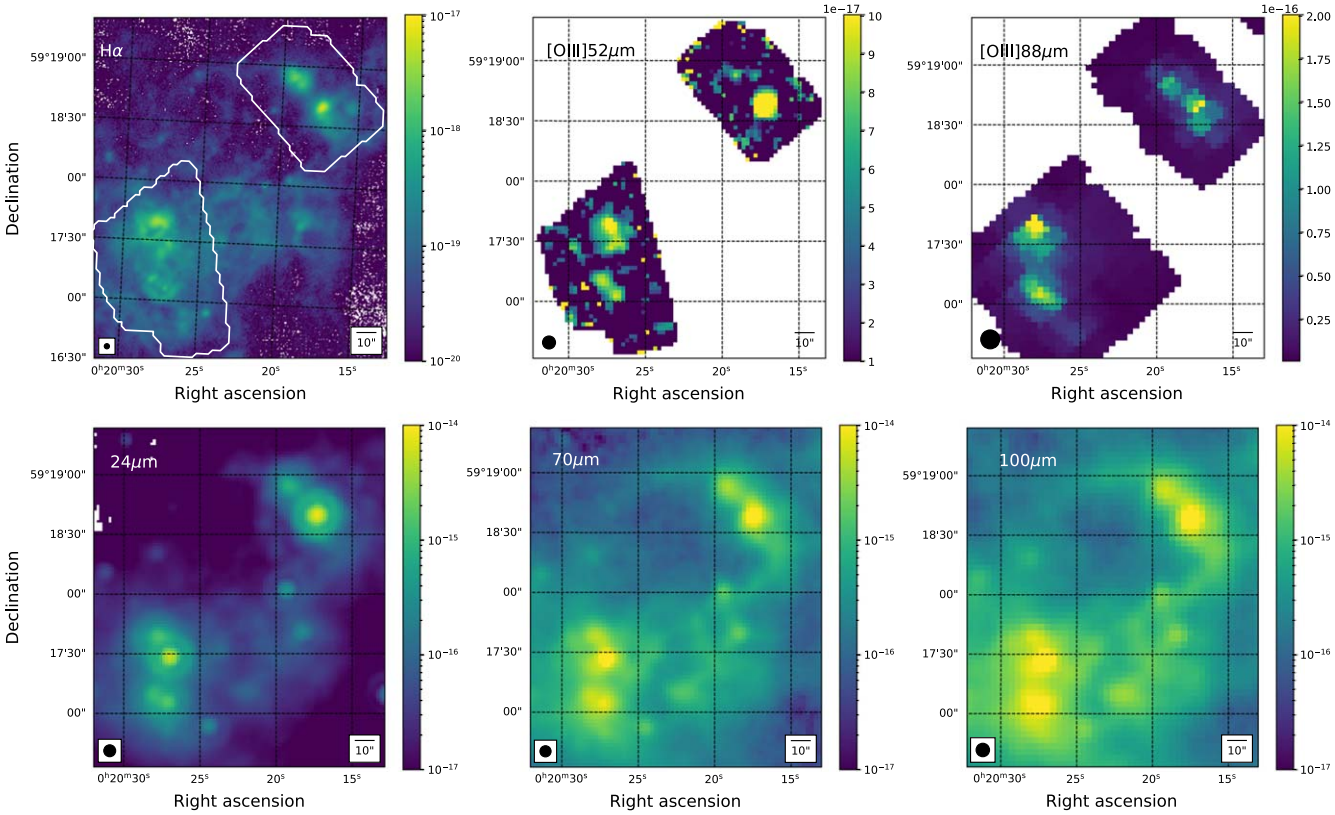

Figure 1. Intensity maps (watts per square meter per pixel) of IC 10. Top: Hα map with the regions observed in [O III] λ52 μm delineated in white (left), [O III] λ52 μm map (middle), [O III] λ88 μm map (right). Bottom: 24 μm map (left), 70 μm map (middle) and 100 μm map (right). The black circle in the lower left corner of each map corresponds to the beam of each observation. The spatial resolution is about 2.″2 for Hα, 6.″6 for [O III] λ52 μm, 9.″5 for [O III] λ88 μm, 6.″0 for 24 μm, 5.″6 for 70 μm, and 6.″8 for 100 μm.

Table 2
Properties of the IR Cooling Lines Used

Line	Wavelength (μm)	IP[a] (eV)	n_{cr}[b] (cm^{-3})	T_{exc} (K)
[S III]	18.7	23.34	2×10^4	769
[S III]	33.5	23.34	7×10^3	430
[O III]	51.8	35.12	3.6×10^3	278
[O III]	88.4	35.12	510	163

Notes.
[a] IP, i.e., the energy necessary to create the ion.
[b] Critical density for collision with electrons.

The field on the bright spot in the northwestern submap was integrated for a total time of about 1 hr, while the other fields were integrated for about 1.5 hr each. The spectral resolution at [O III] λ52 μm is $R = 791$, and the point-spread function has a size of 6.″6 (Fadda et al. 2023; corresponding to ≈23.1 pc) assuming a diffraction-limited telescope.

2.1.2. Data Reduction, Atmospheric Correction, and Calibration

The data have been reduced with the FIFI-LS data reduction pipeline (Vacca et al. 2020) using the calibration products described in Fadda et al. (2023). We applied a kernel size of 0.5× FWHM and a window size of 1.5× FWHM, which ensures that the spatial resolution is conserved. The output cube is sampled at 2″ spatially and 40 km s^{-1} spectrally. Atmospheric absorption may have a significant impact on the observed flux, even at the high altitudes of the flights, between 39,000 and 45,000 feet. To correct the data for the atmospheric absorption, the pipeline creates a transmission spectrum for the local conditions (altitude, elevation, and water vapor overburden) for the observed nod cycle. Since the water vapor overburden was not continuously observed, we used satellite-derived values rescaled to direct measurements obtained during each flight between different observations (Iserlohe et al. 2021; Fischer et al. 2021). The reduced cube has been corrected by the atmospheric absorption factor estimated at the wavelength corresponding to the position of [O III] λ52 μm using SOSPEX[11] (Fadda & Chambers 2018; Fadda 2024), avoiding overcorrection of the wing of the [O III] λ52 μm line, which falls into a deep telluric line. The absolute amplitude calibration uncertainty is assumed to be 15%, of which 10% is relative uncertainty from FIFI-LS seen between flight series and different calibrators. The rest arises from atmospheric corrections and calibration modeling uncertainties. The total intensity map of [O III] λ52 μm is shown in Figure 1 for illustrative purposes only. We estimated the integrated fluxes of [O III] λ52 μm and [O III] λ88 μm directly from the cube (see Section 3.1).

2.2. Ancillary Data

2.2.1. MIR and FIR Data

IC 10 has been mapped in the IR also by Spitzer and by Herschel (Dwarf Galaxy Survey (DGS); Madden et al. 2013) covering the MIR and FIR, respectively. The MIR Spitzer/Infrared Spectrograph (IRS; Houck et al. 2004) and FIR

[11] https://github.com/darioflute/sospex

Herschel/PACS (Poglitsch et al. 2010) spectroscopy data have been presented in Polles et al. (2019). We are particularly interested in bringing into this study the two [S III] maps observed with the Spitzer/IRS low-resolution (LR) modules and the Herschel/PACS [O III] λ88 μm data (Figure 1), which, when combined with [O III] λ52 μm, can be used to derive the electron density (see Section 3). While the [S III] IRS maps have been taken from Polles et al. (2019; see Section 3.1 of Polles et al. 2019 for the details of the data reduction), we re-reduced the PACS [O III] λ88 μm data using the transient correction pipeline available in HIPE 15 (see details in Fadda et al. 2016), which calibrates the flux using the telescope background as an absolute calibrator and corrects for transients. Comparing the reduced [O III] λ88 μm map with the Hα map (Section 2.2.2), we noticed that the astrometry of PACS/[O III] λ88 μm was incorrect by a few arcseconds. Similar astrometric discrepancies have been seen in other PACS data, such as NGC 2146 and M100 (see, e.g., Fadda et al. 2023). We corrected the PACS/[O III] λ88 μm astrometry by using the Hα map.

We complement these observations, which trace the gas properties, with dust continuum observations. The latter data are used to derive additional properties of the H II regions, such as dust temperature. The dust emission of IC 10 has been observed by Spitzer/MIPS and Herschel/PACS. In this paper we only consider the 24, 70, and 100 μm bands. These data have been retrieved from the DustPedia (Davies et al. 2017) database.[12] Since IC 10 is at low Galactic latitude, $b = -3.^{\circ}3$, the continuum maps are contaminated by galactic cirrus, requiring a careful foreground correction. For each photometric image, we calculated the average foreground and the corresponding uncertainty ($\sigma_{\rm fg}$), taking the median and the median absolute deviation (MAD) of the lowest fluxes of the map, the "tail." We identified the "tail" of the emission using an iterative procedure. First, we estimated the median and the MAD of all of the fluxes lower than an arbitrary limit, excluding the fluxes with a distance to the median higher than three MAD. Then we estimated the median again and the MAD of the remaining fluxes. This procedure has been performed until the value of the median converged (see Appendix A). For each map, the corresponding contamination has been subtracted pixel by pixel.

2.2.2. Hα

The Hα map of IC 10 has been obtained by Hunter & Elmegreen (2004a) as part of a sample of 94 irregular galaxies. Several telescopes and instruments have been used to build the Hα catalog of this sample. IC 10 has been observed using the Perkins Telescope at the Lowell Observatory at a spatial resolution of 2.″2, and the reduced and continuum subtracted Hα map has been given to us by the authors. We refer to Hunter & Elmegreen (2004a) for the details of the reduction. In this study, we use the Hα map not corrected for extinction.

3. Electron Density

We used two electron density diagnostics: the line ratio [O III] λ88 μm/[O III] λ52 μm tracing the electron density range between 10 and 10^3 cm^{-3} and the line ratio [S III] λ33 μm/[S III] λ18 μm tracing the electron density range between 100 and 10^4 cm^{-3}. With the derived values, we investigated the distribution of the electron density inside the H II regions of IC 10.

3.1. Electron Density Using the Diagnostic [O III] Line Ratios

The spatial resolution of the [O III] maps (6.″6 for [O III] λ52 μm and 9.″5 for [O III] λ88 μm; see Table 1) does not allow us to resolve individual H II regions; therefore, we identified larger regions, three of which are inside the main star-forming region of IC 10, M1, M1b, and M2, and two regions inside the arc, A1 and A2. For each region, we calculated the electron densities, $n_{\rm e\ [O\ III]}$, inside concentric circular areas in order to investigate the trends of the electron density. The selected circular regions with radii of 6.″4 (∼22.4 pc, c1), 9.″6 (∼36.6 pc, c2), and 12.″8 (∼44.8 pc, c3), are shown in Figure 2.

The [O III] λ52 μm cube was convolved to the same spatial resolution of the [O III] λ88 μm cube. We then extracted the integrated spectrum in each circular aperture using SOSPEX (Fadda & Chambers 2018; Fadda 2024). We fitted the [O III] λ52 μm and [O III] λ88 μm emission lines with a Gaussian and a Voigt profile, respectively, assuming a constant value for the continuum. The fitting is weighted by the spectrum error. The integrated fluxes and the associated line-fit uncertainties are presented in Table 3. Once the fluxes were estimated, we calculated the [O III] ratio and derived the electron density, $n_{\rm e\ [O\ III]}$, using the code PyNeb[13] (Luridiana et al. 2015) with its default atomic database[14] (Morisset et al. 2020). While we assumed a temperature of 9700 K to calculate the electron density (see Appendix B), the [O III] ratio is relatively insensitive to temperature, and therefore to the variations in temperature (e.g., Spinoglio et al. 2015; Kewley et al. 2019a). The variation in the predicted line ratios due to the uncertainty in the temperature is shown with the gray background in Figure 3. The uncertainties of $n_{\rm e\ [O\ III]}$ are dominated by the uncertainties in the [O III] ratio, which have been estimated taking into account the line-fit uncertainties and the calibration uncertainties (15% for [O III] λ52 μm and 12% for [O III] λ88 μm). Table 4 presents the $n_{\rm e\ [O\ III]}$ values, while Figure 3 shows the derived [O III] ratio on the electron density curve.

The derived $n_{\rm e\ [O\ III]}$ covers a range between 10 and 1370 cm^{-3}. Even though the densities derived for each subregion are compatible within the uncertainties, we can identify few trends of the $n_{\rm e\ [O\ III]}$ values as a function of the area. The region with the highest $n_{\rm e\ [O\ III]}$ values is A2. The $n_{\rm e\ [O\ III]}$ value of A2 decreases as the integrated area increases, indicating that, at the spatial resolution of 9.″5, A2 is a point source, and by increasing the integrated area, we are including gas with lower density. The same behavior is shown by the region A1, even though in this case high uncertainties are associated with the derived $n_{\rm e\ [O\ III]}$ values. The second-densest region is M1b. The estimated $n_{\rm e\ [O\ III]}$ of this region and that of M2 are almost constant as the area is increased. The lack of a variation of $n_{\rm e\ [O\ III]}$ suggests that at least at the spatial resolution of 9.″5, the regions M1b and M2 include H II regions larger than the circle "c1" and "c2." Finally, the derived $n_{\rm e\ [O\ III]}$ values of M1 increase as the integrated area increases, showing an opposite trend to what we would expect in

[12] http://dustpedia.astro.noa.gr

[13] http://research.iac.es/proyecto/PyNeb

[14] Several atomic databases are available on PyNeb. The default atomic data set is PYNEB_21_01. The atomic data for O^{++} are from Froese Fischer & Tachiev (2004) and Storey et al. (2014); for S^{++}, Froese Fischer et al. (2006).

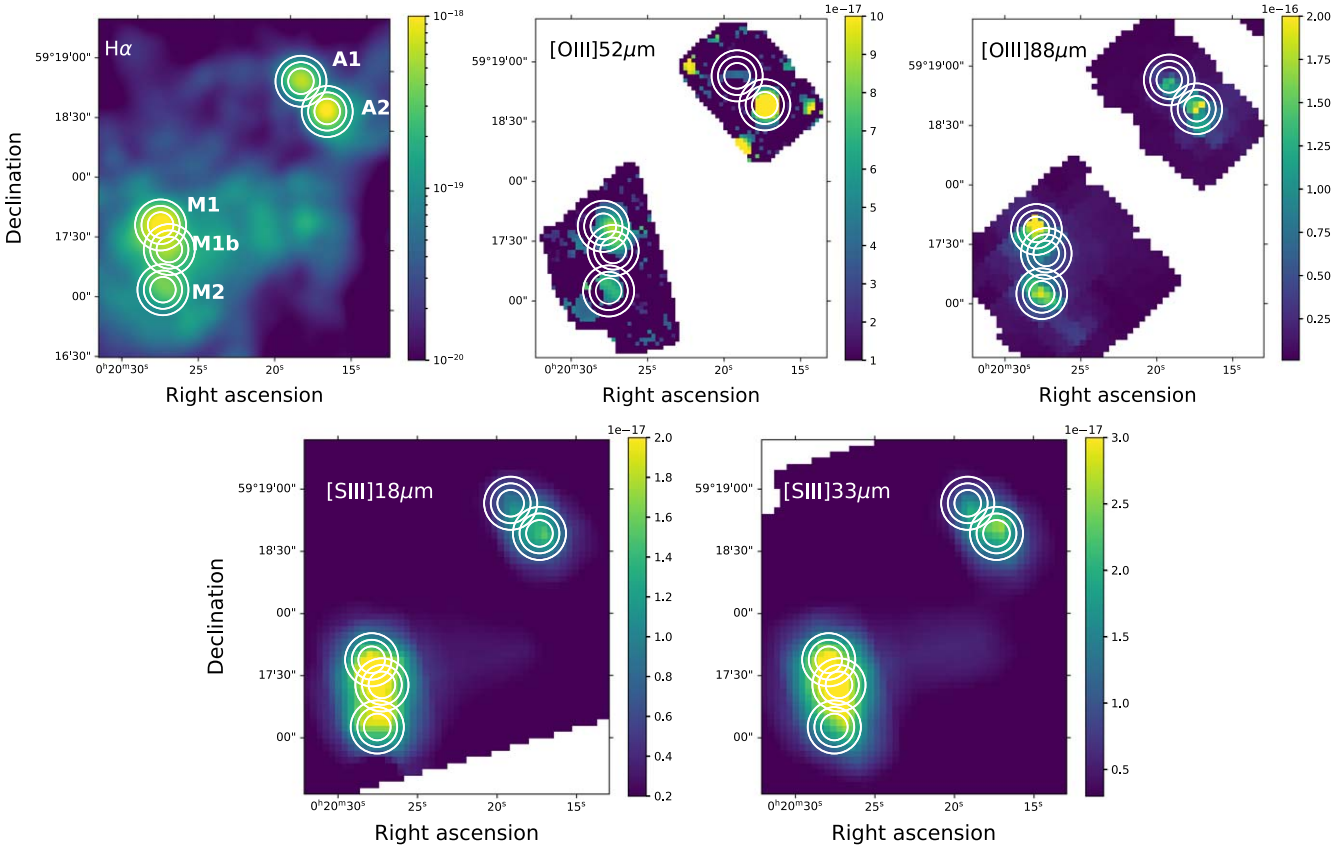

Figure 2. The white circles indicating the regions and subregions described in Section 3 overlap with the intensity maps (watt per square meter per pixel) of IC 10. Top: Hα map (left), [O III] λ52 μm map (middle), [O III] λ88 μm map (right). All three maps are shown at the spatial resolution of 9.″5. Bottom: [S III] λ18 μm map (left) and [S III] λ33 μm map (right), both shown at the spatial resolution of 12″.

Table 3
Integrated fluxes

Name	Region R.A. (J2000)	Region Decl. (J2000)	Radius (arcsec)	Fluxes [O III] λ52 μm (10^{-15}W m^{-2})	Fluxes [O III] λ88 μm (10^{-15} W m^{-2})	Fluxes [S III] λ18 μm (10^{-16} W m^{-2})	Fluxes [S III] λ33 μm (10^{-16} W m^{-2})
M1c1	0:20:27.8835	+59:17:37.523	6.4	1.97 ± 0.06	2.45 ± 0.02	3.46 ± 0.18	4.91 ± 0.36
M1c2	...	...	9.6	4.16 ± 0.13	3.75 ± 0.02	6.59 ± 0.26	9.89 ± 0.54
M1c3	...	...	12.8	6.65 ± 0.27	5.21 ± 0.02	10.16 ± 0.34	15.28 ± 0.68
M1bc1	0:20:27.2390	+59:17:25.400	6.4	2.16 ± 0.15	1.13 ± 0.01	3.21 ± 0.20	5.13 ± 0.49
M1bc2	...	...	9.6	5.01 ± 0.33	2.67 ± 0.02	6.92 ± 0.30	10.60 ± 0.70
M1bc3	...	...	12.8	8.79 ± 0.55	4.73 ± 0.02	11.51 ± 0.39	17.20 ± 0.87
M2c1	0:20:27.5330	+59:17:05.082	6.4	1.62 ± 0.06	1.78 ± 0.01	2.54 ± 0.19	3.20 ± 0.39
M2c2	...	...	9.6	3.33 ± 0.15	3.41 ± 0.02	5.44 ± 0.28	7.32 ± 0.60
M2c3	...	...	12.8	4.54 ± 0.31	4.88 ± 0.02	9.31 ± 0.37	12.61 ± 0.79
A1c1	0:20:19.1184	+59:18:52.981	6.4	0.84 ± 0.09	1.02 ± 0.01	1.44 ± 0.17	2.61 ± 0.35
A1c2	...	...	9.6	1.24 ± 0.16	1.68 ± 0.01	2.96 ± 0.24	4.58 ± 0.47
A1c3	...	...	12.8	1.79 ± 0.28	2.51 ± 0.02	4.67 ± 0.30	6.95 ± 0.58
A2c1	0:20:17.3062	+59:18:38.423	6.4	4.71 ± 0.20	1.86 ± 0.01	2.09 ± 0.17	3.45 ± 0.37
A2c2	...	...	9.6	6.28 ± 0.32	3.11 ± 0.02	4.28 ± 0.24	7.08 ± 0.52
A2c3	...	...	12.8	7.72 ± 0.56	4.32 ± 0.03	6.49 ± 0.31	10.72 ± 0.64

the presence of a compact H II region. The behavior shown by M1 suggests that by increasing its area, we are including H II regions with higher $n_{e\,[O\,III]}$ than that of M1c1, rather than gas with lower density.

3.2. Electron Density Using the Diagnostic [S III] Line Ratio

The integrated [S III] fluxes have been calculated from the Spitzer/IRS LR maps. We integrated the fluxes using the same circular aperture used to calculate the [O III] integrated fluxes. For each integrated flux, the associated uncertainty is the square root of the sum of the squares of the uncertainty map values inside the region. The integrated fluxes and their uncertainties are presented in Table 3. Once the fluxes were estimated, we calculated the [S III] ratio and derived the electron density, $n_{e\,[S\,III]}$, using the code PyNeb and assuming a temperature of 9700 K. The uncertainties on the estimated $n_{e\,[S\,III]}$ are due to the uncertainties on the ratio, while the

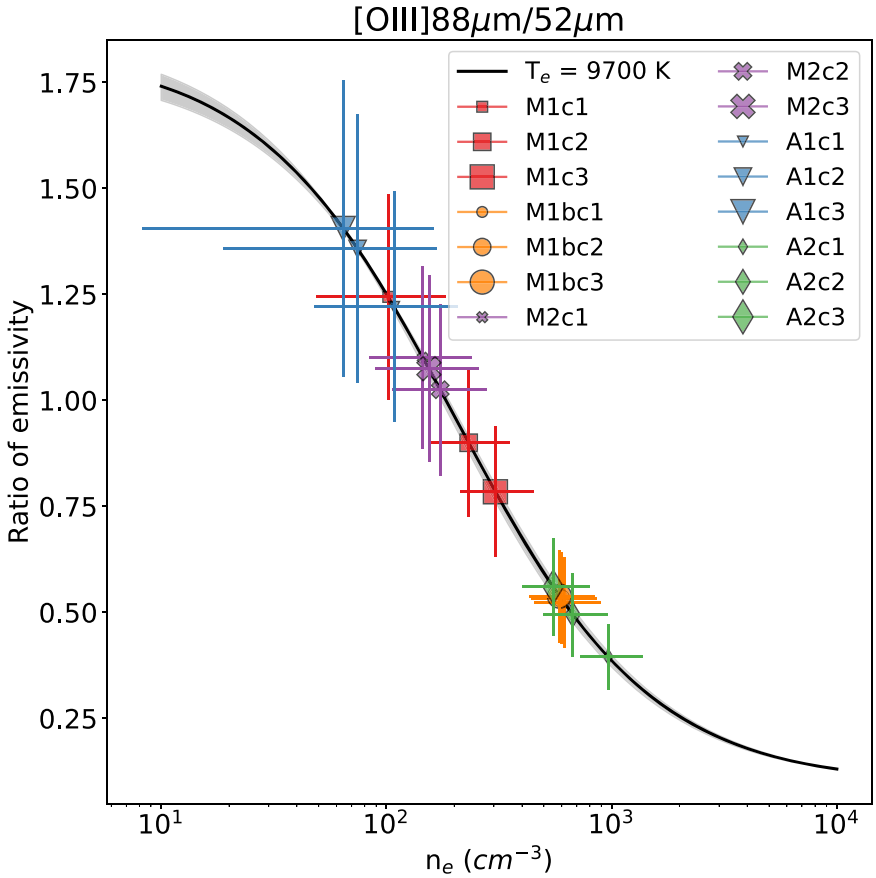

Figure 3. Theoretical ratios of [O III] λ88 μm/[O III] λ52 μm toward different regions of IC 10 (Figure 2), determined at the temperature of 9700 K as a function of the electron density n_e. The different symbols indicate the observed line-ratio values. Each color and symbol corresponds to one region, and the sizes of the symbol increase as the area considered for the integrated flux ratios increases. The gray area shows the uncertainty due to the temperature's uncertainty: the range is between $10^{3.89}$ and $10^{4.07}$ K.

Table 4
Derived Electron Density for $T_e = 9700$ K

Region	$n_{e\ [O\ III]}$ (cm^{-3})	$n_{e\ [S\ III]}$ (cm^{-3})
M1c1	100^{+80}_{-50}	$\mathbf{300}^{+100}_{-80}$
M1c2	230^{+120}_{-80}	250^{+80}_{-70}
M1c3	300^{+150}_{-90}	250^{+70}_{-60}
M1bc1	610^{+270}_{-160}	200^{+110}_{-80}
M1bc2	$\mathbf{600}^{+260}_{-160}$	240^{+90}_{-70}
M1bc3	$\mathbf{590}^{+260}_{-150}$	$\mathbf{260}^{+80}_{-60}$
M2c1	140^{+90}_{-60}	400^{+180}_{-130}
M2c2	170^{+100}_{-70}	340^{+120}_{-90}
M2c3	150^{+100}_{-60}	$\mathbf{340}^{+100}_{-80}$
A1c1	110^{+100}_{-60}	120^{+150}_{-100}
A1c2	70^{+90}_{-60}	230^{+130}_{-90}
A1c3	60^{+100}_{-50}	260^{+110}_{-90}
A2c1	960^{+410}_{-240}	180^{+120}_{-90}
A2c2	670^{+290}_{-170}	180^{+90}_{-70}
A2c3	550^{+250}_{-150}	180^{+80}_{-60}

uncertainties on the temperature are negligible. Figure 4 shows the measured [S III] ratio on the electron density curve, while Table 4 presents the derived $n_{e\ [S\ III]}$ values.

The derived $n_{e\ [S\ III]}$ values cover a range between 30 and 570 cm^{-3}, narrower than that covered by $n_{e\ [O\ III]}$, and there is not a clear trend of $n_{e\ [S\ III]}$ with the size of the aperture for any of the regions. In light of the uncertainties on $n_{e\ [S\ III]}$, all of the derived $n_{e\ [S\ III]}$ values are compatible with each other.

3.3. Electron Density Stratification

Figure 5 shows the comparison between $n_{e\ [S\ III]}$ and $n_{e\ [O\ III]}$ for each subregion (c1, c2, and c3). The relation between $n_{e\ [O\ III]}$ and $n_{e\ [S\ III]}$ is not the same for all of the regions. We can identify two categories: (I) Regions with $n_{e\ [O\ III]}$ always higher than $n_{e\ [S\ III]}$: M1b and A2, the two regions with the highest $n_{e\ [O\ III]}$. For these two regions, the result suggests that the gas traced by the [S III] ratio and the gas traced by the [O III] ratio arise from different components of the ionized gas. The highest density is traced by the ions with the highest IP (35.12 eV for the [O III] line versus 23.34 eV for [S III]), suggesting that the densest clouds are closer to the ionizing source. (II) Regions with $n_{e\ [O\ III]} \sim n_{e\ [S\ III]}$, within the uncertainties: M1, M2, and A1. In these cases, there is no clear density stratification, and both [O III] and [S III] ratios trace gas of similar conditions.

4. Discussion

In Section 3, we found that $n_{e\ [S\ III]}$ is almost uniform between the H II regions analyzed, while $n_{e\ [O\ III]}$ covers a broad range. In the following, we investigate if any of these

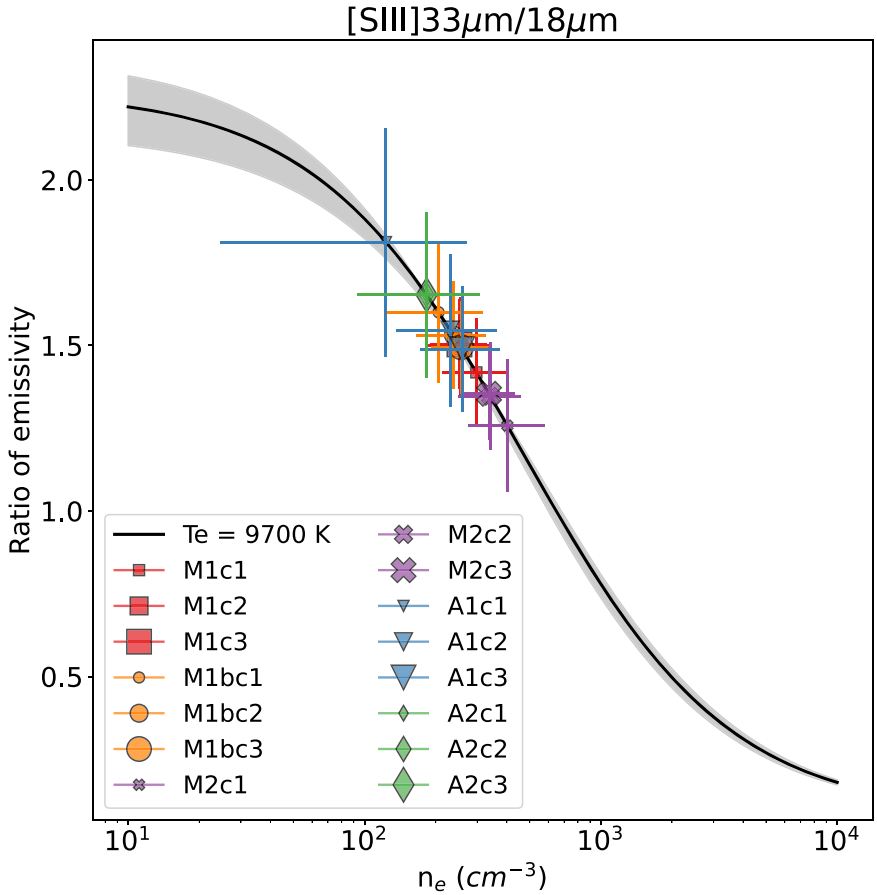

Figure 4. Theoretical ratio [S III] λ33 μm/[S III] λ18 μm at the temperature of 9700 K as a function of the electron density n_e. The symbols indicate the observed line-ratio values. The gray area shows the uncertainty due to the temperature's uncertainty: the range is between $10^{3.89}$ and $10^{4.07}$ K.

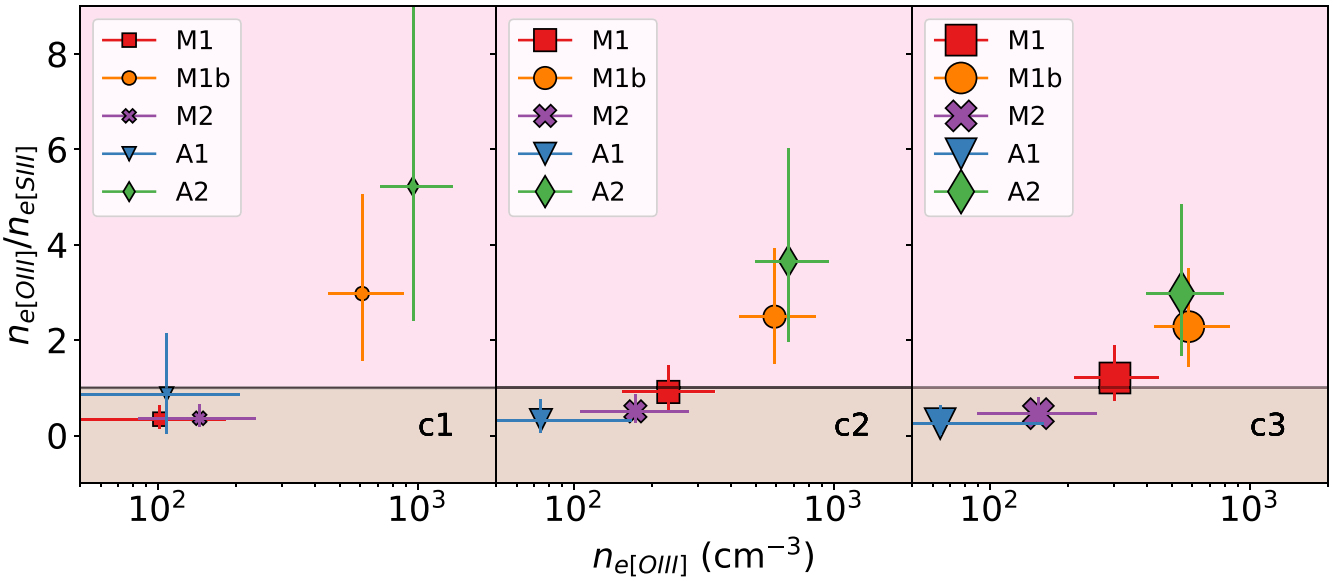

Figure 5. $n_{e\ [O\ III]}/n_{e\ [S\ III]}$ ratio vs. $n_{e\ [O\ III]}$ values for different integrating areas (from left to right, c1, c2, and c3). The color code and symbols are the same as Figure 3.

behaviors correlates with the strength and the hardness of the radiation field of the H II regions and their evolutionary stages. The correlations are quantified using Spearman's rank correlation coefficient calculated with the Python function scipy. stats. spearmanr.

4.1. Electron Density and Radiation Field

The combination of the optical line emission Hα and the dust emission at 24 μm is one of the most reliable tracers of star formation rate (SFR; Kennicutt et al. 2007, 2009). While both the Hα and 24 μm are typically due to heating by young

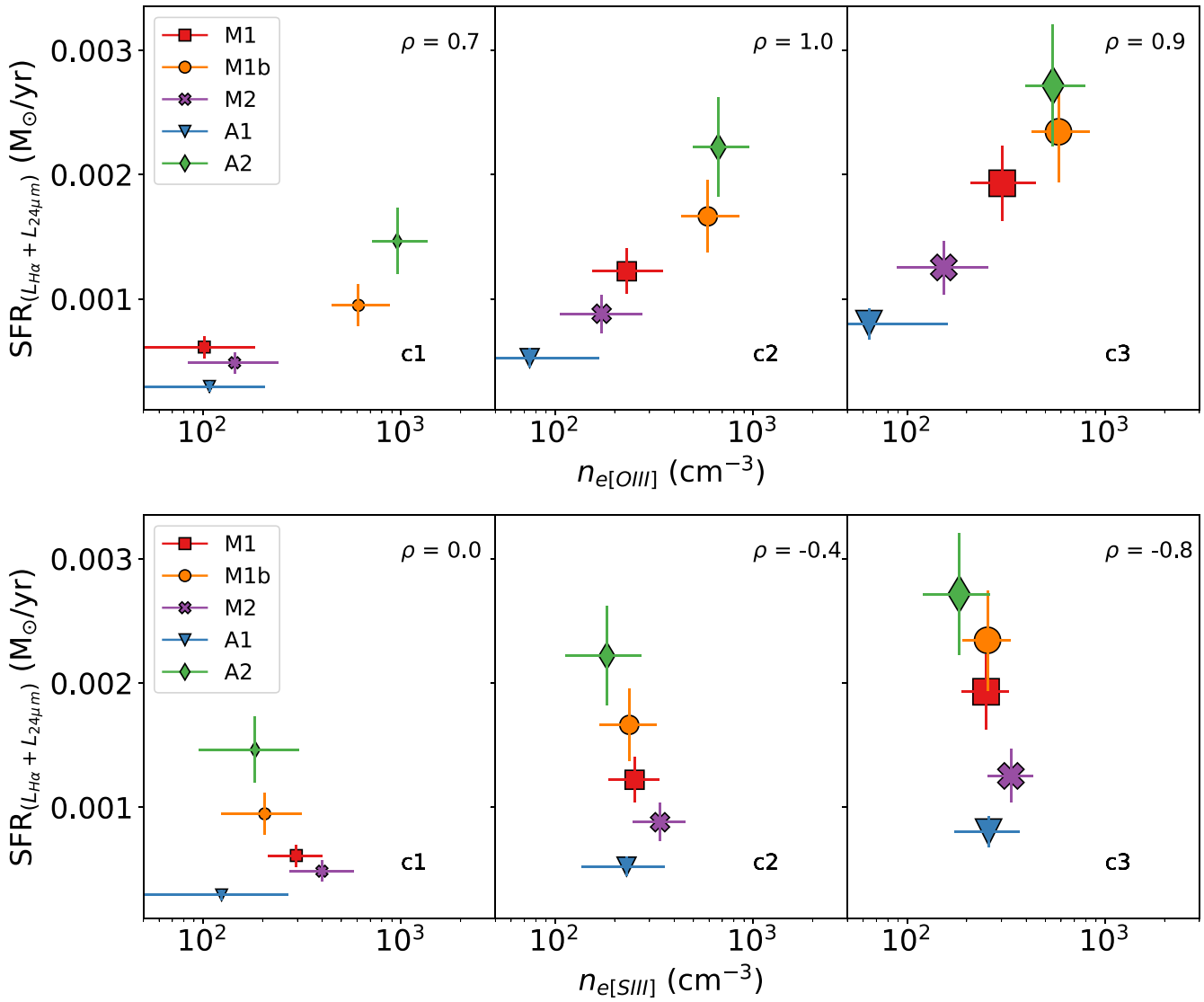

Figure 6. SFR vs. $n_{e\ [O\ III]}$ (top) and SFR vs. $n_{e\ [S\ III]}$ (bottom) for different integrating areas (from left to right, c1, c2, and c3). The color code and symbols are the same as Figure 3. Spearman's rank correlation coefficient is indicated in the top right corner (ρ).

massive stars, they trace different evolutionary stages of the H II regions. Hα is a good tracer of unobscured H II regions, while the 24 μm band is a good tracer of the ongoing dust-obscured star formation (SF). Thus, both Hα and 24 μm are needed to estimate the total SF activity (Calzetti et al. 2007):

$$\mathrm{SFR}(M_\odot \mathrm{yr}^{-1}) = 5.3 \times 10^{-42}[L(\mathrm{H}\alpha)_{\mathrm{obs}}(\mathrm{erg\ s}^{-1}) + (0.031 \pm 0.006)L(24\ \mu\mathrm{m})(\mathrm{erg\ s}^{-1})] \quad (1)$$

where $L(\mathrm{H}\alpha)_{\mathrm{obs}}$ is the observed luminosity of Hα, not corrected for extinction. After convolving both maps to the spatial resolution of 9.″5, we calculated the integrated fluxes of Hα and 24 μm for each subregion (see Table 5) and calculated the corresponding SFR using Equation (1). Figure 6 shows a clear correlation between SFR and $n_{e\ [O\ III]}$, for all the subregions (ρ equal to 0.7, 1.0, and 0.9 for c1, c2, and c3, respectively), while the SFR does not seem to correlate ($\rho = 0.0$), or it is anticorrelated (-0.4 and -0.8) with $n_{e\ [S\ III]}$. Given the uncertainties in the values of $n_{e\ [S\ III]}$, all of the values are consistent with one another. These results suggest that only the electron density traced by O^{++}, the ion with the highest IP, is linked to the SFR: higher $n_{e\ [O\ III]}$ could indicate higher SFR.

We can also investigate a possible correlation between the hardness of the radiation field, the shape of the stellar spectrum, and n_e by examining an indicator of dust temperature, such as the dust continuum ratio 70 μm/100 μm. The dust emission at shorter wavelengths becomes enhanced when the grains are exposed to harder interstellar radiation fields (e.g., Madden et al. 2006). Therefore, we can use the ratio of two IR photometric bands such as 70 μm/100 μm to trace the hardness of the radiation field and investigate its correlation with $n_{e\ [O\ III]}$ and $n_{e\ [S\ III]}$. The integrated fluxes of the 70 μm and 100 μm continua have been estimated following the same procedure used to calculate the [S III] fluxes after convolving both maps to the spatial resolution of 9.″5. Figure 7 shows that the 70 μm/100 μm ratio correlates with $n_{e\ [O\ III]}$ with a correlation coefficient of 0.6, 0.9, and 0.6 for c1, c2, and c3, respectively. These correlations confirm that $n_{e\ [O\ III]}$ is linked to the hardness of the radiation field. Again, given the uncertainties in the values of $n_{e\ [S\ III]}$, no trend in the 70 μm/100 μm ratio with $n_{e\ [S\ III]}$ can be reliably discerned.

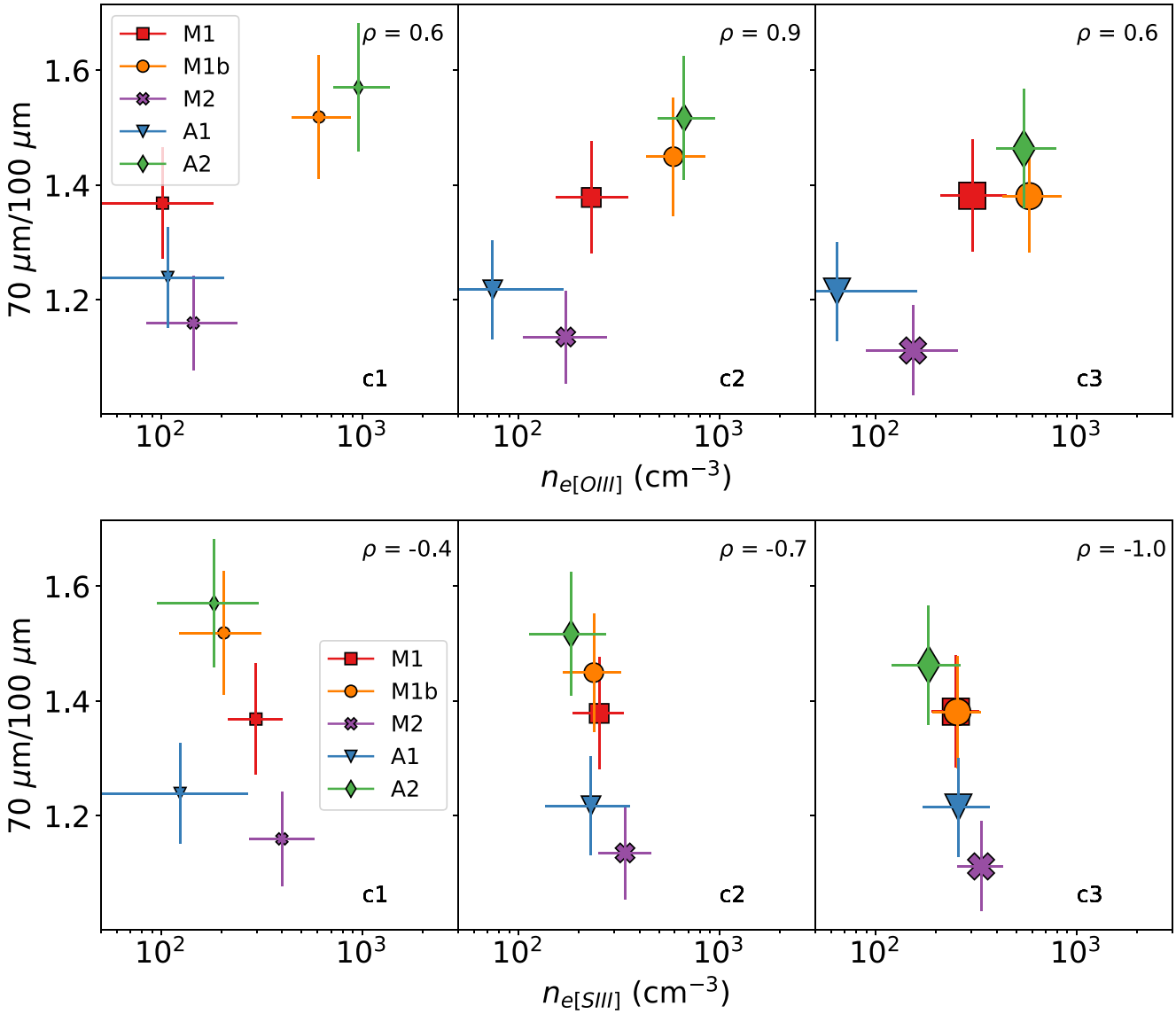

Figure 7. The dust continuum ratio 70 μm/100 μm vs. $n_{e\ [O\ III]}$ (top) and vs. $n_{e\ [S\ III]}$ (bottom). The color code and symbols are the same as Figure 3. Spearman's rank correlation coefficient is indicated in the top right corner (ρ).

Therefore, the electron density traced by the ions with high IP, O^{++}, traces the properties of the radiation field. The results of this study suggest that $n_{e\ [O\ III]}$ reflects the density of the gas layer most affected by the stellar feedback processes and the evolutionary stage of the H II regions, while the electron density of the second layer, traced by the [S III] ratio, is not affected by the variation of the radiation field.

4.2. Embedded H II Regions

In this section, we focus on the young H II regions at early stages of their evolution: the compact H II regions that are still embedded. We are not using $n_{e\ [S\ III]}$ for this analysis since from Section 4.1 it is clear that this quantity does not correlate with other local physical properties of the H II regions.

At the onset of the star formation, the ISM that has not yet been exposed to the stellar feedback is full of dust. These H II regions are therefore bright in 24 μm but not in Hα, which is extincted by dust. In Kim et al. (2021), for example, 24 μm has been used to measure the duration of the earliest embedded phase of star formation. Figure 8 shows the 24 μm luminosity versus $n_{e\ [O\ III]}$ (top panel) and the Hα luminosity versus $n_{e\ [O\ III]}$ (bottom panel). Each panel contains the results for one of the subregions (c1, c2, and c3). This figure highlights a clear correlation between the 24 μm luminosity and the $n_{e\ [O\ III]}$ for all of the subregions (ρ equal to 0.7, 1.0, and 0.9 for c1, c2, and c3, respectively) and a lower correlation between the observed Hα luminosity and the $n_{e\ [O\ III]}$ ($\rho = -0.1$ in the case of c1 and $\rho = 0.6$ for c2 and c3). The brightest regions in 24 μm are A2 and M1b, while the brightest region in the observed Hα is M1. These results indicate that the densest H II regions in $n_{e\ [O\ III]}$ are also the dustiest. Moreover, the low correlation between Hα and $n_{e\ [O\ III]}$ suggests that the latter is a good tracer of the young embedded star-forming regions, while it is a less efficient tracer for evolved star-forming regions.

From the previous results, it is clear that the A2 region is a more extreme region than the other H II regions of IC 10. A2 stands out in that it is very bright in [O III] λ52 μm and in all of the dust emission tracers, especially at 24 μm. In addition, the $n_{e\ [O\ III]}$ value is much higher than those of the other H II

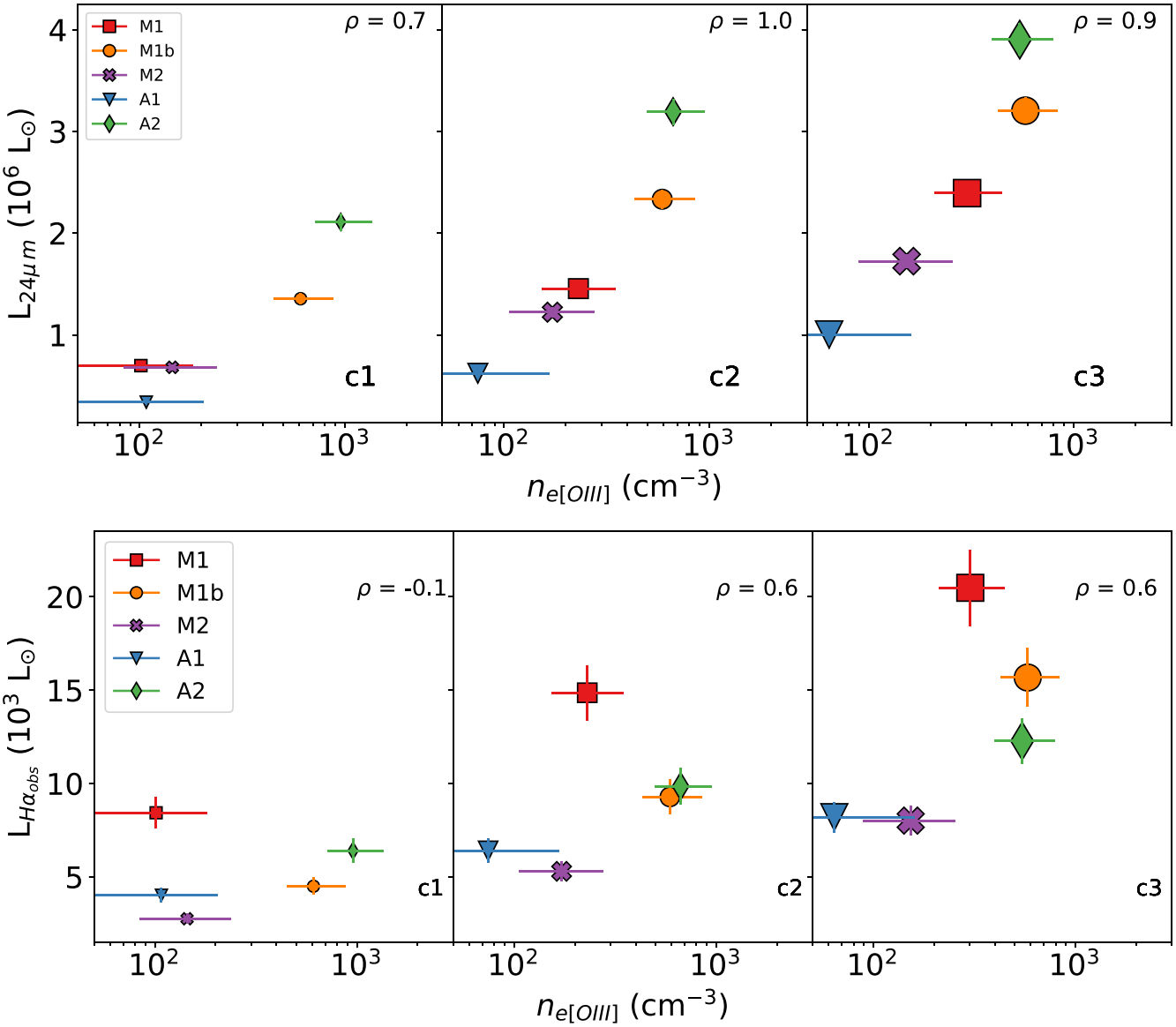

Figure 8. 24 μm luminosity vs. $n_{e\ [O\ III]}$ values (top) and observed Hα luminosity vs. $n_{e\ [O\ III]}$ values (bottom). Left: c1 subregions; middle: c2 subregions; right: c3 subregions. Spearman's rank correlation coefficient is indicated in the top right corner (ρ).

regions. These characteristics suggest that A2 is an embedded dense H II region. This conclusion is confirmed by the radio continuum emission. A2 is the brightest source with e-MERLIN observations in 5 and 1.5 GHz by Westcott et al. (2017). The authors classified A2 as a compact H II region, combining 5 and 1.5 GHz data with Hα and 70 μm (see Figure 3 of Westcott et al. 2017).

The young age of the H II region A2 is also supported by the presence of an early-nitrogen-sequence type of WR star (WNE) at its center (see Figure 9). The WR stars are the post-main-sequence stage of the high-mass O stars, and the WNE is the first phase of a WR. All of this leads to a picture of A2 as a young embedded dense H II region with a massive WNE at its center, which is too young to have dispersed the surrounding dust with its feedback. Higher angular resolution data (e.g., GMOS data, Tehrani et al. 2017; KCWI data, Cosens et al. 2022) show that, among the several WR stars of IC 10 (see Figure 9), three of these are situated inside an H II region: the aforementioned WNE at the center of A2, the O2.5 If/WN6 inside M1c1, and the WC4 inside M2c2. The KCWI data shows that the O2.5 If/WN6 star is located at the edge of the H II region (Figure 26 of Cosens et al. (2022)). The notation O2.5 If/WN6 indicates a star in the intermediate stage between an O2.5 and a WN6 star. The young evolutionary stage of this WR star and its position suggest that this star is a product of a second generation of star formation associated with the evolved H II region complex inside M1c1. This scenario would agree with the bright emission in Hα and the low emission in 24 μm of M1c1. The WC4 star inside M2c2 is located at the center of a compact H II region that is visible with high spatial resolution (Figure 26 of Cosens et al. 2022) but with emission diluted at the spatial resolution of c2 (19.″6). Moreover, the WC4 designation indicates a WR star that is more evolved than a WNE star. Therefore, A2 is unique in hosting an early-stage WN at its center.

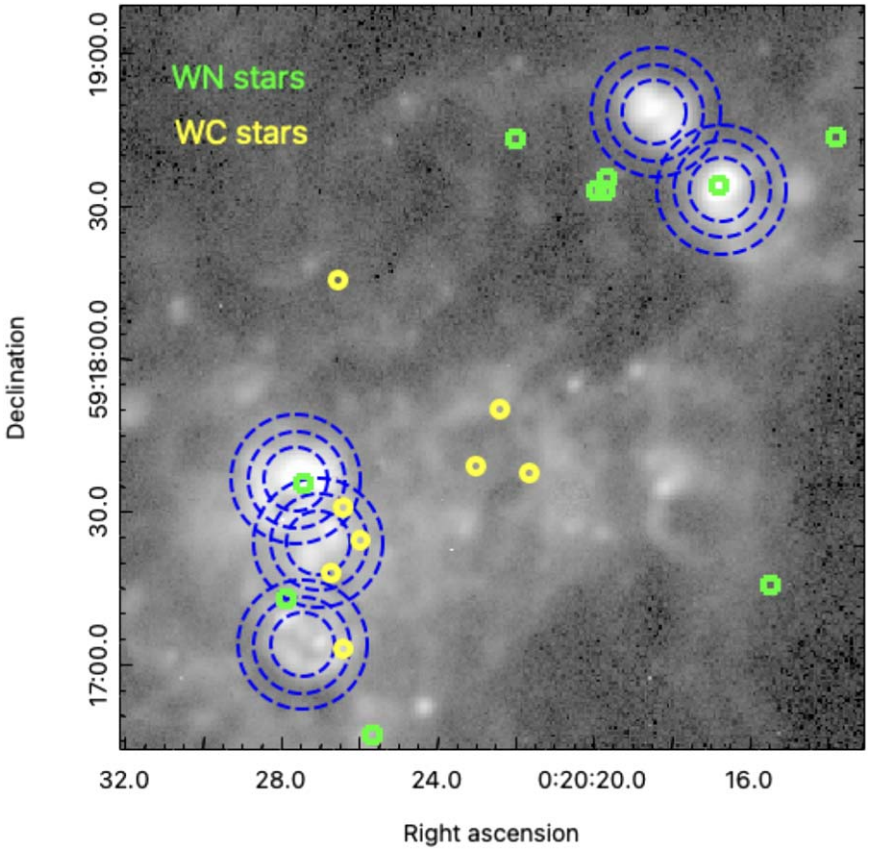

Figure 9. Hα image of IC 10 with the positions of the WR stars from Tehrani et al. (2017) overlaid. The regions analyzed in this study are indicated with blue circles.

Table 5
Integrated fluxes

Region	Hα[a] (10^{-16} W m^{-2})	24 μm[b] (10^{-14} W m^{-2})	70 μm[b] (10^{-13} W m^{-2})	100 μm[b] (10^{-13} W m^{-2})
M1 c1	5.30	4.38 ± 0.02	1.041 ± 0.004	0.761 ± 0.002
M1 c2	9.34	9.14 ± 0.04	2.187 ± 0.007	1.587 ± 0.004
M1 c3	12.90	15.04 ± 0.05	3.682 ± 0.010	2.665 ± 0.005
M1b c1	2.83	8.52 ± 0.05	2.211 ± 0.011	1.456 ± 0.005
M1b c2	5.83	14.67 ± 0.06	3.817 ± 0.013	2.633 ± 0.007
M1b c3	9.85	20.14 ± 0.06	5.344 ± 0.013	3.870 ± 0.007
M2 c1	1.73	4.28 ± 0.01	1.542 ± 0.004	1.330 ± 0.003
M2 c2	3.33	7.68 ± 0.02	2.862 ± 0.005	2.520 ± 0.004
M2 c3	5.04	10.84 ± 0.02	4.192 ± 0.006	3.770 ± 0.005
A1 c1	2.52	2.12 ± 0.01	0.670 ± 0.003	0.541 ± 0.002
A1 c2	4.02	3.91 ± 0.01	1.201 ± 0.004	0.987 ± 0.003
A1 c3	5.15	6.30 ± 0.02	1.796 ± 0.006	1.478 ± 0.004
A2 c1	4.02	13.26 ± 0.08	2.469 ± 0.017	1.573 ± 0.009
A2 c2	6.19	20.08 ± 0.09	3.830 ± 0.019	2.525 ± 0.011
A2 c3	7.72	24.53 ± 0.09	4.771 ± 0.019	3.261 ± 0.011

Notes.
[a] Observed, not corrected. We assume a flux's uncertainty of 10%.
[b] The foreground uncertainties (4×10^{-19} W m^{-2}, 1×10^{-17} W m^{-2}, and 2×10^{-17} W m^{-2}, for 24 μm, 70 μm and 100 μm, respectively) are negligible in comparison with the uncertainties of the fluxes.

5. Summary

We combined our [O III] λ52 μm SOFIA/FIFI-LS data with Herschel/PACS [O III] λ88 μm data and the [S III] λ18 μm and [S III] λ33 μm data from Spitzer/IRS to investigate the electron density of the brightest H II regions of the nearby dwarf galaxy IC 10 at different spatial resolution: 44.8 pc (c1), 73.2 pc (c2), and 89.6 pc (c3).

The range of values covered by the derived $n_{e\ [O\ III]}$ is broad, between 10 and 1370 cm^{-3}. For the regions A1 and A2, the derived $n_{e\ [O\ III]}$ decreases when considering larger areas, suggesting that those are point sources, at the spatial resolution of 9.″5. In the case of M1, $n_{e\ [O\ III]}$ increases when the area is enlarged. This different behavior can be explained by the fact that the M1 region is made up of several H II regions. We identified the center of the H II regions based on the Hα luminosity, and in the case of M1, it seems that the position of the peak in Hα emission does not correspond to the densest H II region of the area.

The electron densities derived using the [S III] ratio are more uniform than those derived from the [O III] ratio. The $n_{e\ [S\ III]}$ values are between 30 cm^{-3} and 570 cm^{-3}. Comparing $n_{e\ [O\ III]}$ with $n_{e\ [S\ III]}$, we found that for two regions, M1b and A2, the [O III] and the [S III] ratios trace different components of the ionized gas, while for the other regions, i.e., M1, M2, and A1, $n_{e\ [O\ III]} \sim n_{e\ [S\ III]}$ is traced across the different subregions. These results indicate that the distribution of the gas components inside the H II region is not straightforward. Our study suggests that the electron density distribution gives us information about the evolutionary stage of the H II region. In the case of A2, a confirmed embedded compact H II region hosting a WNE star at the center, the highest density is traced by the [O III] line ratio, with O^{++} being the ion with the highest IP (35 eV), indicating that the densest clouds are closer to the ionizing source. On the other side, $n_{e\ [O\ III]} \sim n_{e\ [S\ III]}$ in unobscured H II regions such as M1. This hypothesis is

supported by the discovery that $n_{e\,[O\,III]}$ correlates with the 24 μm emission, which traces the embedded young SF activity.

Finally, we found that $n_{e\,[O\,III]}$ correlates with SFR and dust temperature. Thus, the electron density traced by [O III] is also an indicator of the hardness and the intensity of the radiation field, with higher $n_{e\,[O\,III]}$ found in more energetic environments, while the gas layers traced by [S III] do not depend on the properties of the radiation field.

IC 10 has been the pilot galaxy to study the electron density stratification inside H II regions using the IR [S III] and [O III] line ratios. To verify if the conclusions inferred studying the H II regions of IC 10 are valid in general, it will be necessary to expand the analysis to a heterogeneous sample of nearby galaxies, thereby providing a quantitative understanding of the environmentally dependent interplay between stars and gas. Galaxies that have been observed with integral-field unit such as Very Large Telescope/MUSE (Bacon et al. 2010), CFHT/SITELLE (Drissen et al. 2019), or JWST/MIRI (Rieke et al. 2015) would be the ideal objects for these followup studies.

Acknowledgments

We wish to thank the anonymous referee for providing insightful comments, which helped to improve this paper. This paper was based on observations made with the NASA/DLR Stratospheric Observatory for Infrared Astronomy (SOFIA) and with Herschel. SOFIA was jointly operated by the Universities Space Research Association, Inc. (USRA), under NASA contract NNA17BF53C, and the Deutsches SOFIA Institut (DSI) under DLR contract 50 OK 0901 to the University of Stuttgart. M.C. and L.R. gratefully acknowledge funding from the DFG through an Emmy Noether Research Group (grant No. CH2137/1-1). COOL Research DAO is a Decentralized Autonomous Organization supporting research in astrophysics aimed at uncovering our cosmic origins.

Facilities: SOFIA (FIFI-LS), Herschel (MIPS, PACS), Spitzer (IRS), Perkins.

Software: astropy (Astropy Collaboration et al. 2013, 2018, 2022), Cloudy (Ferland et al. 2013), SOSPEX (Fadda & Chambers 2018; Fadda 2024).

Appendix A
Estimate of the Foreground Cirrus Contamination

Figure 10, left panel, shows the increasing distribution of all of the fluxes of the continuum 24 μm map. The small window inside the plot shows the zoom on the section of the distribution where the emission starts to increase drastically. The upper limit of the final "tail" identified with the iterative procedure described in Section 2 is shown with a black line, while the red line corresponds to the median value, i.e., foreground emission. The right panel of Figure 10 shows the pixels with a flux value higher than the upper limit of the "tail." Figures 11 and 12 show the same as Figure 10 but for the continua 70 μm and 100 μm, respectively.

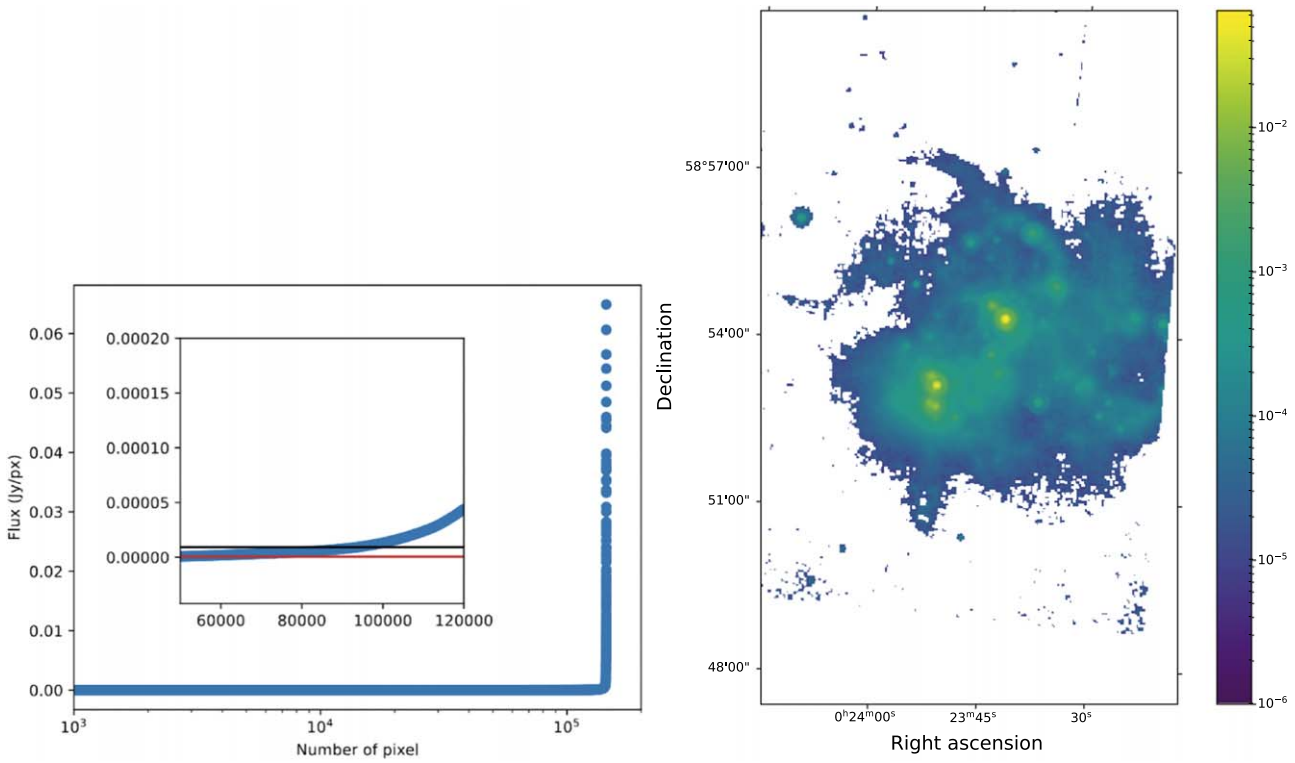

Figure 10. Left: increasing distribution of the 24 μm fluxes, with a zoom on the distribution showing the point where the emission starts to increase rapidly. The black line shows the upper limit of the fluxes used to calculate the foreground emission, while the red line corresponds to the derived foreground emission. Right: map of the continuum 24 μm emission showing only the pixels with a flux higher than the upper limit used to identify the "tail" (black line on the plot on the left).

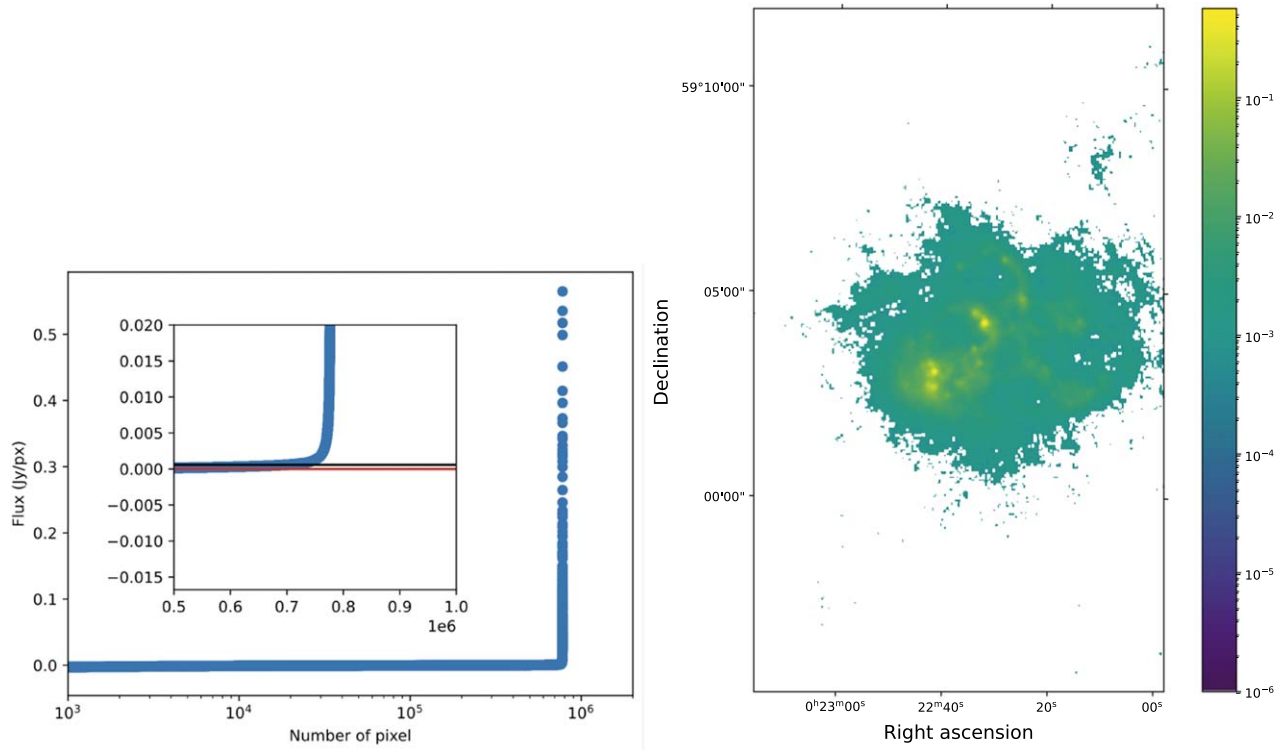

Figure 11. Left: increasing distribution of the 70 μm fluxes, with a zoom on the distribution showing the point where the emission starts to increase rapidly. The black line shows the upper limit of the fluxes used to calculate the foreground emission, while the red line corresponds to the derived foreground emission. Right: map of the continuum 70 μm emission showing only the pixels with a flux higher than the upper limit used to identify the "tail" (black line on the plot on the left).

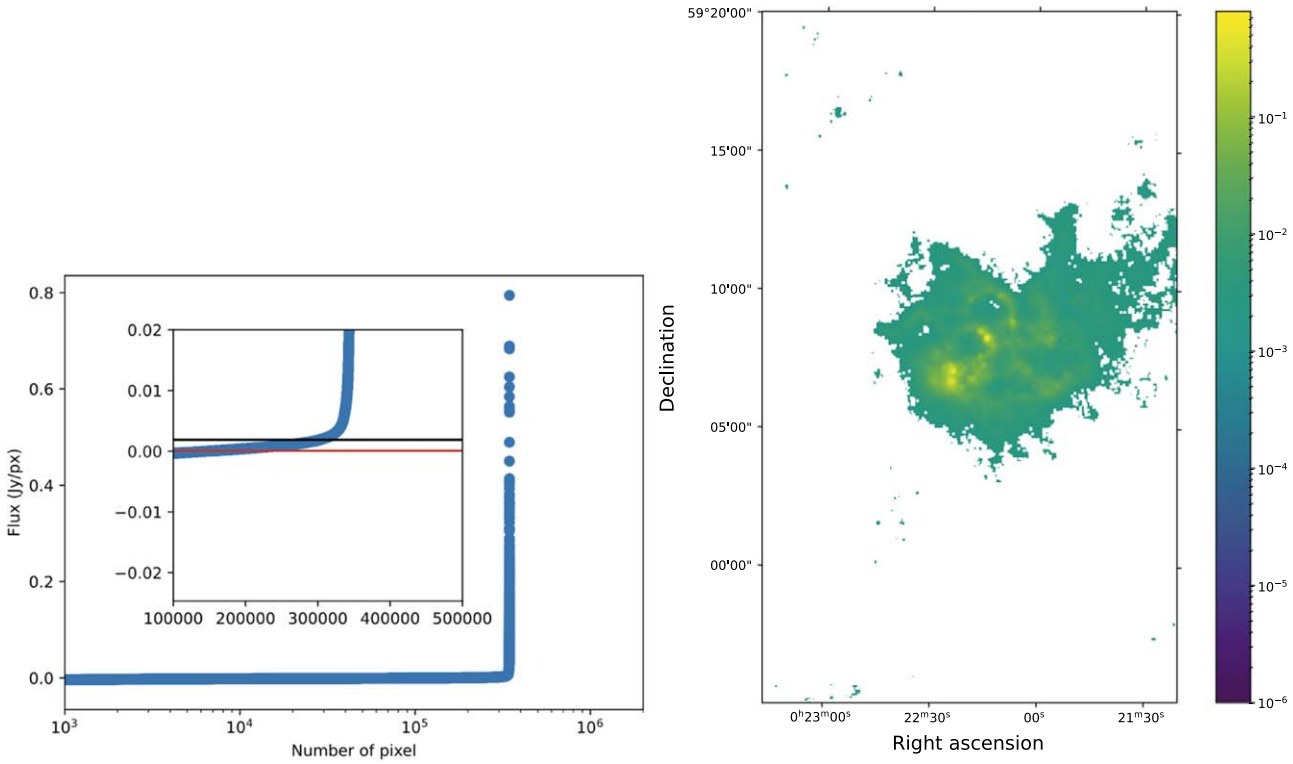

Figure 12. Left: increasing distribution of the 100 μm fluxes, with a zoom on the distribution showing the point where the emission starts to increase rapidly. The black line shows the upper limit of the fluxes used to calculate the foreground emission, while the red line corresponds to the derived foreground emission. Right: map of the continuum 100 μm emission showing only the pixels with a flux higher than the upper limit used to identify the "tail" (black line on the plot on the left).

Appendix B
Temperature Variation

The low energy of the transition of the IR fine-structure levels compared to the gas temperature makes these ratios relatively insensitive to temperature, except in the low-density limit (e.g., Osterbrock & Ferland 2006; Kewley et al. 2019b). The IR [O III] ratio and the [S III] ratio are sensitive to the temperature variation for $n_e < 10^{1.9}$ cm^{-3} and $n_e < 10^{2.5}$cm^{-3}, respectively. Since the gas temperature is affected by the metallicity, with colder temperatures for a H II region with higher metallicity, the same dependency of the derived $n_{e\,[O\,III]}$ and $n_{e\,[S\,III]}$ seen for the gas temperature can be seen for the metallicity (see Figures 3, 15, and 16 of Kewley et al. 2019a). Deriving the exact temperature corresponding to the metallicity requires a complete photoionization modeling. Since those models have been already performed and presented in Polles et al. (2019) for each investigated region (i.e., M1, M1b, M2, A1, and A2), we extracted the information of the gas temperature from the corresponding best-model result. Figure 13 shows the behavior of the temperature as a function of the depth of the H II region for each of those models. We estimate the electron density using 9700 K, the median temperature of the range covered by those five gas profiles before reaching the ionization front (where the temperature drops off) from $10^{3.89}$ to $10^{4.07}$ K. Figures 3 and 4 show with a gray area the uncertainty range corresponding to the gas temperature range.

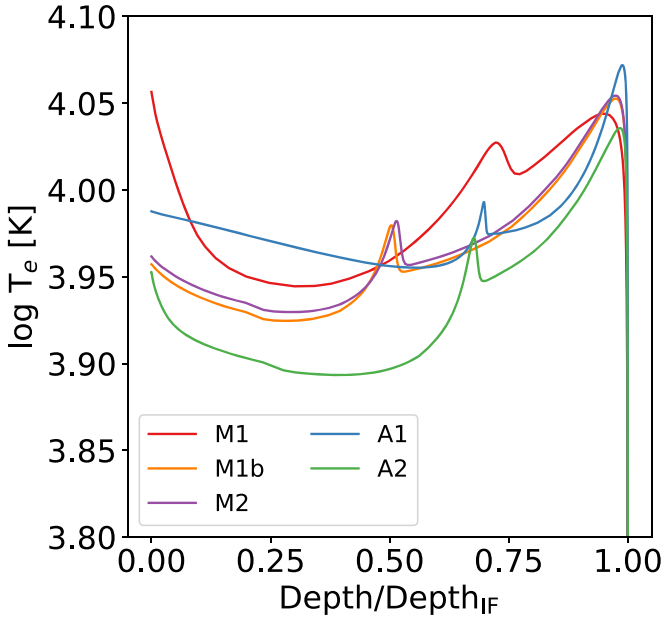

Figure 13. Gas temperature profiles calculated by the best-model solution of each of the H II regions studied. The depth is normalized to the value reached at the ionization front (Depth$_{IF}$).

ORCID iDs

Fiorella L. Polles https://orcid.org/0000-0003-0347-3201
Dario Fadda https://orcid.org/0000-0002-3698-7076
William D. Vacca https://orcid.org/0000-0002-9123-0068
Nicholas P. Abel https://orcid.org/0000-0003-1791-723X
Mélanie Chevance https://orcid.org/0000-0002-5635-5180
Christian Fischer https://orcid.org/0000-0002-7299-8661
James M. Jackson https://orcid.org/0000-0002-3466-6164
Vianney Lebouteiller https://orcid.org/0000-0002-7716-6223
Suzanne Madden https://orcid.org/0000-0003-3229-2899
Lise Ramambason https://orcid.org/0000-0002-9190-9986

References

Ashley, T., Elmegreen, B. G., Johnson, M., et al. 2014, AJ, 148, 130
Astropy Collaboration, Robitaille, T. P., Tollerud, E. J., et al. 2013, A&A, 558, A33
Astropy Collaboration, Price-Whelan, A. M., Lim, P. L., et al. 2022, ApJ, 935, 167
Astropy Collaboration, Price-Whelan, A. M., Sipőcz, B. M., et al. 2018, AJ, 156, 123
Bacon, R., Accardo, M., Adjali, L., et al. 2010, Proc. SPIE, 7735, 773508
Calzetti, D., Kennicutt, R. C., Engelbracht, C. W., et al. 2007, ApJ, 666, 870
Chevance, M., Madden, S. C., Fischer, C., et al. 2020, MNRAS, 494, 5279
Colditz, S., Beckmann, S., Bryant, A., et al. 2018, JAI, 7, 1840004
Cosens, M., Wright, S. A., Murray, N., et al. 2022, ApJ, 929, 74
Crowther, P. A., Drissen, L., Abbott, J. B., Royer, P., & Smartt, S. J. 2003, A&A, 404, 483
Davies, J. I., Baes, M., Bianchi, S., et al. 2017, PASP, 129, 044102
Della Bruna, L., Adamo, A., Bik, A., et al. 2020, A&A, 635, A134
Drissen, L., Martin, T., Rousseau-Nepton, L., et al. 2019, MNRAS, 485, 3930
Erickson, E. F., & Davidson, J. A. 1993, AdSpR, 13, 549
Fadda, D. 2024, SOSPEX, v1.0.4, Zenodo, doi:10.5281/zenodo.11302120
Fadda, D., & Chambers, E. T. 2018, AAS Meeting Abstracts, 231, 150.11
Fadda, D., Colditz, S., Fischer, C., et al. 2023, AJ, 166, 237
Fadda, D., Jacobson, J. D., & Appleton, P. N. 2016, A&A, 594, A90
Ferland, G. J., Porter, R. L., van Hoof, P. A. M., et al. 2013, RMxAA, 49, 137
Fernández-Ontiveros, J. A., Spinoglio, L., Pereira-Santaella, M., et al. 2016, ApJS, 226, 19
Fischer, C., Beckmann, S., Bryant, A., et al. 2018, JAI, 7, 1840003
Fischer, C., Bryant, A., Beckmann, S., et al. 2016, Proc. SPIE, 9910, 991027
Fischer, C., Iserlohe, C., Vacca, W., et al. 2021, PASP, 133, 055001
Froese Fischer, C., & Tachiev, G. 2004, ADNDT, 87, 1
Froese Fischer, Charlotte, Tachiev, Georgio, & Irimia, Andrei 2006, ADNDT, 92, 607
Hodge, P., Smith, T., Eskridge, P., MacGillivray, H., & Beard, S. 1991, ApJ, 379, 621
Houck, J. R., Roellig, T. L., van Cleve, J., et al. 2004, ApJS, 154, 18
Hunter, D., & Elmegreen, B. G. 2004a, AJ, 128, 2170
Iserlohe, C., Fischer, C., Vacca, W. D., et al. 2021, PASP, 133, 055002
Kaasinen, M., Bian, F., Groves, B., Kewley, L. J., & Gupta, A. 2017, MNRAS, 465, 3220
Keenan, F. P., Feibelman, W. A., & Berrington, K. A. 1992, ApJ, 389, 443
Kennicutt, R. C. J., Calzetti, D., & Walter, F. 2007, ApJ, 671, 333
Kennicutt, R. C. J., Hao, C.-N., Calzetti, D., et al. 2009, ApJ, 703, 1672
Kepley, A. A., Bittle, L., Leroy, A. K., et al. 2018, ApJ, 862, 120
Kewley, L. J., Nicholls, D. C., Sutherland, R., et al. 2019a, ApJ, 880, 16
Kewley, L. J., Nicholls, D. C., & Sutherland, R. S. 2019b, ARA&A, 57, 511
Kim, J., Chevance, M., Kruijssen, J. M. D., et al. 2021, MNRAS, 504, 487
Kim, M., Kim, E., Hwang, N., et al. 2009, ApJ, 703, 816
Lequeux, J., Peimbert, M., Rayo, J. F., Serrano, A., & Torres-Peimbert, S. 1979, A&A, 80, 155
López-Sánchez, Á. R., Mesa-Delgado, A., López-Martín, L., & Esteban, C. 2011, MNRAS, 411, 2076
Luridiana, V., Morisset, C., & Shaw, R. A. 2015, A&A, 573, A42
Madden, S. C., Galliano, F., Jones, A. P., & Sauvage, M. 2006, A&A, 446, 877
Madden, S. C., Rémy-Ruyer, A., Galametz, M., et al. 2013, PASP, 125, 600
Magrini, L., & Gonçalves, D. R. 2009, MNRAS, 398, 280
Massey, P., & Holmes, S. 2002, ApJL, 580, L35
McLeod, A. F., Gritschneder, M., Dale, J. E., et al. 2016, MNRAS, 462, 3537
Méndez-Delgado, J. E., Esteban, C., García-Rojas, J., Kreckel, K., & Peimbert, M. 2024, NatAs, 8, 275-277
Méndez-Delgado, J. E., Esteban, C., García-Rojas, J., et al. 2023, MNRAS, 523, 2952
Morisset, C., Luridiana, V., García-Rojas, J., et al. 2020, Atoms, 8, 66
Nussbaumer, H., & Schild, H. 1979, A&A, 75, L17
O'Dell, C. R., Ferland, G. J., & Peimbert, M. 2017, MNRAS, 464, 4835
Osterbrock, D. E., & Ferland, G. J. 2006, in Astrophysics of Gaseous Nebulae and Active Galactic Nuclei, ed. University Science Books (Herndon, VA: Univ. Science Books)
Peng, B., Lamarche, C., Stacey, G. J., et al. 2021, ApJ, 908, 166
Pineda, J. L., Horiuchi, S., Anderson, L. D., et al. 2019, ApJ, 886, 1

Poglitsch, A., Waelkens, C., Geis, N., et al. 2010, A&A, 518, L2
Polles, F. L., Madden, S. C., Lebouteiller, V., et al. 2019, A&A, 622, A119
Rickards Vaught, R. J., Sandstrom, K. M., Belfiore, F., et al. 2024, ApJ, 966, 130
Rieke, G. H., Wright, G. S., Böker, T., et al. 2015, PASP, 127, 584
Rubin, R. H. 1989, ApJS, 69, 897
Rubin, R. H., Simpson, J. P., O'Dell, C. R., et al. 2011, MNRAS, 410, 1320
Spinoglio, L., Pereira-Santaella, M., Dasyra, K. M., et al. 2015, ApJ, 799, 21
Spinoglio, L., Fernández-Ontiveros, J. A., Malkan, M. A., et al. 2022, ApJ, 926, 55
Storey, P. J., Sochi, Taha, & Badnell, N. R. 2014, MNRAS, 441, 3028
Tehrani, K., Crowther, P. A., & Archer, I. 2017, MNRAS, 472, 4618
Vacca, W., Clarke, M., Perera, D., Fadda, D., & Holt, J. 2020, in ASP Conf. Ser. 527, Astronomical Data Analysis Software and Systems XXIX, ed. R. Pizzo et al. (San Francisco, CA: ASP), 547
Vacca, W. D., Sheehy, C. D., & Graham, J. R. 2007, ApJ, 662, 272
Westcott, J., Brinks, E., Beswick, R. J., et al. 2017, MNRAS, 467, 2113